Adsorptive and Photocatalytic Properties of Green Synthesized ZnO and ZnO/$NiFe_2O_4$ Nanocomposites for Tannery Wastewater Treatment

J. O. Tijani[1,3*], U. A. Aminu[1,3], M. T. Bankole[1,3], M. M. Ndamitso[1,3], A. S. Abdulkareem[2,3]

[1]Department of Chemistry, Federal University of Technology, Minna, Nigeria.
[2]Department of Chemical Engineering, Federal University of Technology, Minna, Nigeria.
[3]Nanotechnology Research Group, Centre for Genetic Engineering and Biotechnology (CGEB), Federal University of Technology, Minna, Nigeria.

ABSTRACT: This study investigated adsorptive and catalytic behaviour of ZnO and ZnO/$NiFe_2O_4$ nanocomposites for the removal and degradation of organic pollutants in tannery wastewater. ZnO and ZnO/$NiFe_2O_4$ nanomaterials were synthesized via a green method using Zn, Fe and Ni salts precursor and leaves extract of *Anacardium occidentale (linn.)*. Subsequently, the synthesized samples were characterized by different analytical tools. The adsorptive and catalytic performance of the prepared nanomaterial were assessed using reduction in Chemical Oxygen Demand (COD), Biochemical Oxygen Demand (BOD) and Total Organic Carbon (TOC) in tannery wastewater as indicator parameters. High Resolution Scanning Electron Microscope (HRSEM), High Resolution Transmission Electron Microscope (HRTEM), and X-Ray Diffraction (XRD) analysis of ZnO and ZnO/$NiFe_2O_4$ confirmed the formation of hexagonal wurtzite nanoparticle and cubic spinel phase with an average crystallite sizes in the range of 13- 28 nm and 30.44 – 42.53 nm respectively. XRD analysis confirmed no change in the polymorph of ZnO upon the addition $NiFe_2O_4$. XPS spectrum showed the existence of the elements in the following oxidation state (+2) for Zn, (+1, +2) for Ni and (+2 and +3) for Fe. BET analysis revealed order of the specific surface area of ZnO/$NiFe_2O_4$ (44.61 m^2/g) > $NiFe_2O_4$ (40.39 m^2/g) > ZnO (8.91 m^2/g). The adsorptive and photocatalytic results revealed that 3% ZnO/$NiFe_2O_4$ exhibits higher efficiency compared to ZnO and $NiFe_2O_4$ nanoparticles alone and in the order of 3% ZnO/$NiFe_2O_4$ > $NiFe_2O_4$ > ZnO. The study revealed that the prepared nanomaterial behaved better as photocatalyst than as nanoadsorbent.

KEYWORDS: Adsorption, photocatalytic technology; ZnO; ZnO/$NiFe_2O_4$, tannery wastewater

[Received August 31, 2020, Revised Oct. 19, 2020, Accepted Oct. 21, 2020] Print ISSN: 0189-9546 | Online ISSN: 2437-2110

I. INTRODUCTION

Industrial tanning transformation process which deal with the conversion of animal hides and skin into leather generates highly turbid, coloured and foul-smelling wastewater (Hayelom et al., 2014). Tannery wastewater contains highly recalcitrant chemical pollutants such as chromium-complex collagen, surfactants, sulfides, chlorides and salts. In addition, tannery wastewater also contains high concentration of biological oxygen demand (BOD), chemical oxygen demand (COD), total organic carbon (TOC), suspended solids (SS), nitrogen, conductivity, sulfide/sulphates, and chlorides among others (Wosnie et al., 2014). The volume of wastewater produced per ton of raw hide is around 30 – 35 m^3 per day (Abdel et al., 2015). Several conventional methods; coagulation-flocculation, precipitation, oxidation, ion exchange, membrane filtration, ozonation, activated carbon adsorption, biological, and electrodialysis have been utilized to treat tannery wastewater (Asim et al., 2013). These methods have associated shortcomings such as high cost of reagents, generation of toxic sludge, low efficiency, and sometimes, organic pollutants were only transferred from one phase to another and may even become more toxic than the parent compounds (Pawar et al., 2014).

In recent times, heterogeneous photocatalytic technology has received considerable attention among researchers due to their capability to degrade numerous organic contaminants into carbon dioxide and water (Islam et al., 2014). Metal oxides such as, TiO_2, ZnO, WO_3, SiO_2 and Fe_2O_3 can absorb a photon of light to generate free reactive species such as hydroxyl radicals, hydrogen peroxide amongst others. These reactive species selectively attack organic pollutants in wastewater and liberate carbon dioxide and water. Of the aforementioned metal oxide nano catalyst, ZnO nanoparticles has emerged as the leading candidate in photocatalysis due to its availability, excellent chemical stability, non-toxicity and high catalytic activities (Islam et al., 2014; Matinise et al., 2017). ZnO nanoparticles are relatively cheap and can absorb a wide range of UV spectrum compared to other metal oxides. ZnO is classified as an n-type semiconductor with a wide band gap of 3.37 eV, large exciton binding energy of 60 meV and often

*Corresponding author: jimohishola8@gmail.com; jimohtijani@futminna.edu.ng
doi: http://dx.doi.org/10.4314/njtd.v17i4.10

characterized with high thermal and mechanical stability at room temperature (Kumaran et al., 2017).

ZnO nanoparticles can be synthesized by physical and chemical methods such as solvothermal reduction, sol-gel technique, hydrothermal, flame spray pyrolysis, thermal evaporation, chemical vapour deposition, photo deposition, to mention but few (Peruma et al., 2014). However, these methods are costly, generate toxic by-products, require complex synthesis procedure and in most cases required high energy (Manokari et al., 2016). Nowadays, the synthesis of nanoparticles using plants extracts to replace expensive commercial and toxic reducing agents such as $NaBH_4$ or $LiAlH_4$ have been globally recognized as a route to reduce environmental pollution due to availability of plant material, use of less toxic chemicals, eco-friendly nature and one step synthesis of nanoparticles (Hassan, 2015).

ZnO nanoparticles often have high band gap energy and low surface area thus responsible for its low photocatalytic activity in the visible region (Sena and Jainb, 2015). Concerted efforts are ongoing towards the reduction of the band gap of ZnO and extend its absorption threshold to visible region (Suresh and Narayanan, 2013). One of such approaches is doping of ZnO with either metals, non-metals, or metal oxides in most cases addition of both substrates for the suppression of high electron hole recombination rate mostly common to ZnO based catalyst (Snehal et al., 2016). Doping is the anchoring of foreign materials (impurities) onto the ZnO framework to suppress electron-movement from valence band to conduction band (Swaroop, and Somashekarappa, 2015). One of the dopants considered in this study is nickel ferrites ($NiFe_2O_4$). Nickel ferrite is a mixed metal oxide of nickel and iron (III) oxide with Fe as the main component due to its ferromagnetic ordering and magnetism as well as super exchange interaction (Angadi et al., 2016).

Mixed spinel structure ferrites are particularly of interest among researchers, due to its electric, dielectric, and magnetic properties (Hushim et al., 2013). Nickel ferrite belongs to the class of mixed spinel ferrite and shows unexpected properties at nano scale owing to the redistribution of cations (Hushim et al., 2013). Other properties include cation ionic radii, crystal field effect, presence of ion to specific site, ionic charge that causes distribution of cation in mixed spinel ferrites (Hazra and Ghosh, 2014).

In this study, ZnO/$NiFe_2O_4$ nanocomposites were synthesized using combination of green and wet impregnation methods. The synthesized ZnO, $NiFe_2O_4$, ZnO/$NiFe_2O_4$ were analyzed using different characterization tools. The adsorptive and photocatalytic behaviour of synthesized ZnO/$NiFe_2O_4$ nanocomposites for the removal and degradation of organic pollutants in tannery wastewater were also investigated.

II. MATERIALS AND METHODS

A. Materials

The following analytical grade reagents/chemicals; $FeCl_3.6H_2O$, $NiCl_2.6H_2O$, NaOH, Zn $(O_2CCH_3)_2$, HCl and CH_3CH_2OH with percentage purity in the range of 87-99.8% were obtained from Sigma Aldrich and used without further purification. The tannery wastewater was collected from a tannery factory along Tudun Wada area in Sokoto, Sokoto State, Nigeria, and stored in clean polythene bottles. Prior to collection of samples, the bottles were washed with 10% Nitric acid and rinsed with de-ionized water and later stored in a refrigerator prior to analysis. While fresh leaves of *Anacardium occidentale (linn.)* were collected from different location within Minna metropolis and identified in the Department of Biological Sciences Federal University of Technology Minna. The samples were washed to remove dust particles, air dried and pulverized using mortar and pestle to obtain fine powder.

B. Methods

1.) Preparation of Plant Extract for Green Synthesis

Fifty grams of the pulverized Anacardium occidentale (linn.) leaves was weighed into 400 mL of distilled water in a reflux flask and refluxed for 2 h. The extract was filtered using muslin cloth and subsequently with Whatman No. 1 filters paper. The semi-dry extract was weighed, placed in a sterile bottle and stored in a refrigerator until further use (Snehal et al., 2016).

2). Green synthesis of ZnO nanoparticles

ZnO nanoparticles were synthesized via green method using zinc acetate and plant extracts as precursor and reducing agent respectively. To synthesize the ZnO nanoparticles, 0.25 g of zinc acetate was dissolved in 50 mL distilled water; 15 mL aqueous *Anacardium occidentale (linn.)* extract was added. The resulting mixture was stirred for 10 minutes on a magnetic stirrer at constant stirring speed of 200 rpm. 0.2 M of NaOH was added to adjust the pH with continuous stirring, to 10. The solution was further stirred for 2 h followed by the decantation of the supernatant liquid and centrifugation at 3000 rpm for 30 minutes. The formed residue was washed severally with distilled water and subsequently dried in the oven overnight at 60^{o}C. Subsequently, the ZnO cakes formed were calcined in a furnace at 500°C for 2 h (Brintha and Ajitha, 2015)

.

3.) Synthesis of $NiFe_2O_4$ nanoparticles

The procedure employed for the synthesis of nickel ferrite nanoparticles ($NiFe_2O_4$) are described as follows: 15 mL each of 0.4 M $FeCl_3.6H_2O$ and 0.2 M solutions of $NiCl_2.6H_2O$ were measured into 100 mL beaker followed by addition of 5 mL of *Anacardium occidentale (linn.)* extract. The mixture was stirred continuously on a magnetic stirrer for 30 minutes. Then, 0.2 M NaOH solution was added into the mixture with continuous stirring to adjust the pH to 10 and suspensions were formed. The mixture was later stirred for 2 h at 80°C followed by centrifugation to obtain the resulting products which was washed severally with distilled water and ethanol to eliminate unwanted impurities. Later, the precipitates were first dried in an oven at 80^{o}C for 2 h and later calcined at 600^{o}C for 2 h in the furnace to change the amorphous $NiFe_2O_4$ nanoparticles to crystalline phase of $NiFe_2O_4$ (Chen *et al.,* 2016). $NiFe_2O_4$ nanoparticles obtained in this stage were used to prepare the ZnO/$NiFe_2O_4$ nanocomposites.

4.) Synthesis of ZnO/$NiFe_2O_4$

$NiFe_2O_4$/ZnO nanocomposites were synthesized using wet impregnation method described by (Zulfiqar *et al.*, 2015) as follows: 3%, v/v (ZnO) and $NiFe_2O_4$ were dissolved in 40 mL ethanol and then stirred for 30 min. 0.5 M NaOH solution was added dropwise to the mixture until the pH of 10 was achieved and stirred for 1 h. The precipitates formed were washed severally with distilled water and ethanol to eliminate unwanted impurities from the prepared sample. The prepared cake was oven dried at 80°C for 2 h and later calcined at 600°C for 2 h to obtain crystalline 3% ZnO/$NiFe_2O_4$ nanocomposites.

C. Characterization of the Prepared Nanomaterials

The morphology of the prepared ZnO/$NiFe_2O_4$ was determined using Zeiss Auriga High Resolution Scanning Electron Microscopy (HRSEM). The individual element in the samples was examined by energy dispersive spectroscopy via adjustment of the measurement angle of the detector. A Zeiss Auriga HR-TEM, operated at 200 kV was used to examine the microstructure of the prepared samples. The samples were prepared by dispersing approximately 0.04 g in 20 cm^3 in ethanol followed by ultra-sonication for 10 min. A drop of the solution was placed on a holey-carbon copper grid and air dried at room temperature. After exposure to photolight, the copper grids with samples were mounted into the electron microscope for HRTEM and SAED analysis. XRD instrument Bruker AXS Advanced diffractometer with Monochromatic Copper (Cu)-Kα radiation as X-ray source having a wavelength of 0.154 nm was used for phase structure identification, cell dimension and atomic spacing.

The XRD diffractograms were recorded with 2θ range of 20 - 90°, a step size of 0.028°, and operating at 45 kV and 40 mA. The surface area, pore volume and pore size distribution of the prepared samples were determined by Brunauer–Emmett-Teller (N_2 BET) technique using a NOVA 4200e surface area and pore analyzer instrument. The PHI 5400 XPS spectrometer using a non-monochromatic Mg K_α X-ray source (1253.6 eV, 15 kV, and 200 W) and hemispherical sector analyser was used to determine the surface oxidation states of the elements in the nanomaterials. Spectra were analysed using XPS PEAK 4.1 software.

D. Physico-chemical Characterization of Tannery Wastewater

Physico-chemical analysis was carried out on the tannery wastewater before and after the wastewater was treated with the synthesized ZnO, $NiFe_2O_4$ and ZnO/$NiFe_2O_4$ nanomaterial under sunlight irradiation. The collected samples were analyzed for the following parameters; pH, turbidity, sulphate, nitrate and chlorides. pH of the wastewater was determined by electrometric method after calibrating the pH meter with buffer solutions 4 and 7. APHA–2130 B (Nephelometric Method) turbidimeter was used to measure the turbidity. For nitrates and sulphate, colorimetric method was used for their determination with the use of Hach Colorimeter. The following reagents; NitraVer 5 Nitrate pillow, sulphate reagent pillow for nitrate, and sulphate respectively were added to each sample cell containing some wastewater and mixed.

The mixtures were run in the Hach colorimeter, and results were recorded mg/L. Chloride determination was carried out using Argentometric method. Total organic carbon (TOC) was determined using a Shimazu TOC analyser (model 5050A).While soluble Chemical Oxygen Demand (COD) was measured by a closed reflux colorimetric method. The COD reactor was first preheated to 150°C, and 100 mL of wastewater sample was homogenized for 30 seconds in a blender. The homogenized water sample was put in a vial, gently mixed and the vial was placed in the preheated COD reactor. Afterward, the mixture in the vial was cooled to room temperature; the reading was taken in mg/L. The parameters were analyzed using standard procedures reported by previous authors (U.S. Environmental Protection Agency, 2009).

E. Adsorption Experiment

The absorption and photocatalytic activities of the three nanomaterials were carried out as follows: Synthesized ZnO (0.5 g) was added to the wastewater and, the mixture was stirred at 200 rpm for 3 h. 20 mL wastewater was sampled periodically (every 30 minutes) and filtered, and the filtrate was subsequently analyzed for reduction in TOC, BOD, COD and other physico-chemical parameters. This procedure was repeated using $NiFe_2O_4$, 3% ZnO/$NiFe_2O_4$. Another control experiment was conducted by exposing 50 mL tannery wastewater to natural sunlight irradiation alone without the prepared nano catalysts.

F.) Catalytic Activities of the Synthesized Nanocomposites ZnO, $NiFe_2O_4$ and 3% ZnO/$NiFe_2O_4$

The photocatalytic degradation of the organic pollutants in the tannery wastewater by the prepared nanomaterial was evaluated by reduction in TOC, BOD, and COD. The photocatalytic experiments of the synthesized catalyst (ZnO, $NiFe_2O_4$, and 3% $NiFe_2O_4$/ZnO) were performed in a designed photoreactor placed on a magnetic stirrer under natural light from the sun. For each experiment, 1g of the photocatalysts was dispersed in 100 mL of the tannery wastewater. The tannery wastewater and photocatalyst was kept in the dark with continuous stirring for 60 minutes in order to establish the adsorption and desorption process before exposure to sunlight. The mixture was later kept under sunlight and stirred continuously at 200 rpm and the degree of mineralization was monitored for 3 h. 20 mL of the mixture was taken at regular time intervals (0 min, 30 min, 60 min, 90 min, 120 min, and 150 min) centrifuged and filtered using Whatman No. 1 filter paper. This procedure was then repeated using - $NiFe_2O_4$ and 3% ZnO/$NiFe_2O_4$ nanocomposites under the same dosage of 1 g of the catalyst and 100 mL of the tannery wastewater.

G. Data Analysis

The percentage degradation efficiency of BOD was calculated using the formulas in Eqs. (1-3).

$$Eff\ (\%) = \frac{(BOD_0 - BOD_1)}{BOD_0} \times 100 \quad (1)$$

where BOD_o and BOD_1 are the initial and final concentration of BOD in the tannery wastewater respectively. The percentage degradation of COD efficiency was estimated using Eq. (2).

$$Eff\ (\%) = \frac{(COD_0 - COD_1)}{COD_0} \times 100 \quad (2)$$

where COD_o and COD_1 are the initial and final levels of COD in the tannery wastewater respectively. The percentage degradation efficiency of TOC was estimated using Eq. (3).

$$TOC = TC - IC \quad (3)$$

where TC is all the carbon in the sample including organic and inorganic and IC are all inorganic carbon present in the tannery wastewater.

III. RESULTS AND DISCUSSION

A. *Characterization of the Nanomaterials*

The morphology of the prepared samples was examined using HRSEM and their corresponding images are shown in Figure 1.

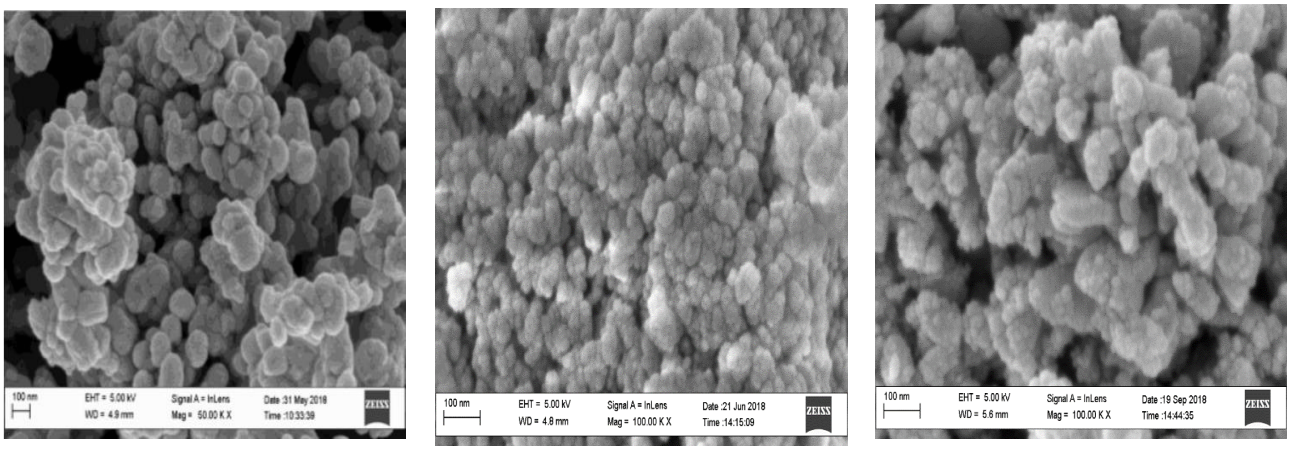

(a) **(b)** **(c)**

Figure 1: HRSEM micrographs of (a) ZnO (b) $NiFe_2O_4$ (c) 3% ZnO/$NiFe_2O_4$ nanocomposites.

Figure 1 (a) revealed the formation of uniformly distributed spherical and hexagonal shaped particles with an average size of 13-28 nm Figure (b), shows densely packed agglomerated spherical structure of $NiFe_2O_4$ nanoparticles with narrow size distribution were observed. The size of the particles was observed to range between 30-42 nm. Figure 1(c) 3% ZnO/$NiFe_2O_4$ showed uniform aggregated spherical morphology with some voids, an indication that $NiFe_2O_4$ were tightly coupled on the surface of ZnO due to the magnetic attraction between nickel ferrite and zinc oxide layers. This favoured the charge transfer between $NiFe_2O_4$ and ZnO and enhanced the separation of photogenerated electron–hole pairs and by extension photocatalytic performance of the ZnO under visible light (Sena *et al.*, 2015; Suresh and Snehal *et al.*, 2016; Narayanan, 2013).

1.) HRTEM/SAED analysis

Microstructural images and their corresponding selected electron diffraction patterns are shown in Figure 2. Figure 2 (a) confirmed the formation of almost hexagonal shape of ZnO nanoparticles with an average particles size in the range of 15-30 nm. The selected area electron diffraction (SAED) patterns of the ZnO nanoparticles (Figure 2 (d)) also revealed the presence of bright spots and lattice fringes. This clearly indicates relatively high crystallinity of ZnO. The diffraction rings pattern is similar to the diffraction peaks in the XRD pattern rings which correspond to (010), (002), (011), (012), (110), and (101) miller indices, respectively. The appearance of bright spot confirmed that the prepared ZnO nanoparticles preferentially formed along the (100) and (101) direction. This however contradict the outcome of Wang *et al.* (2009) who found that ZnO nanoparticles grew along only (001) direction. The differences may be linked to adopted method of preparing ZnO nanoparticles, while Wang and colleagues employed co-precipitation method; this present work utilized green synthesis. In Figure 2 (b), it can be seen that some of the particles were completely spherical in nature while some were elongated and attributed to the spinel nature of the nanoferrites. Some moderately agglomerated particles as well as segregated particles were also present in the sample due to a strong interaction between the Ni and Fe. The estimated average size of the nanoparticles was about 35nm. Selected area electron diffraction pattern of $NiFe_2O_4$ (Figure 2(e)) indicated the presence of distinct ring patterns confirming their nanocrystalline spinel structure. The measured interplanar spacing from selected-area electron diffraction pattern suggested that the prepared $NiFe_2O_4$ were polycrystalline in nature. Zhang *et al.* (2009) reported a rod like morphology of $NiFe_2O_4$ with an average diameter of 100 nm and length of 5 mm respectively. Manikandan *et al.*, (2018) revealed the

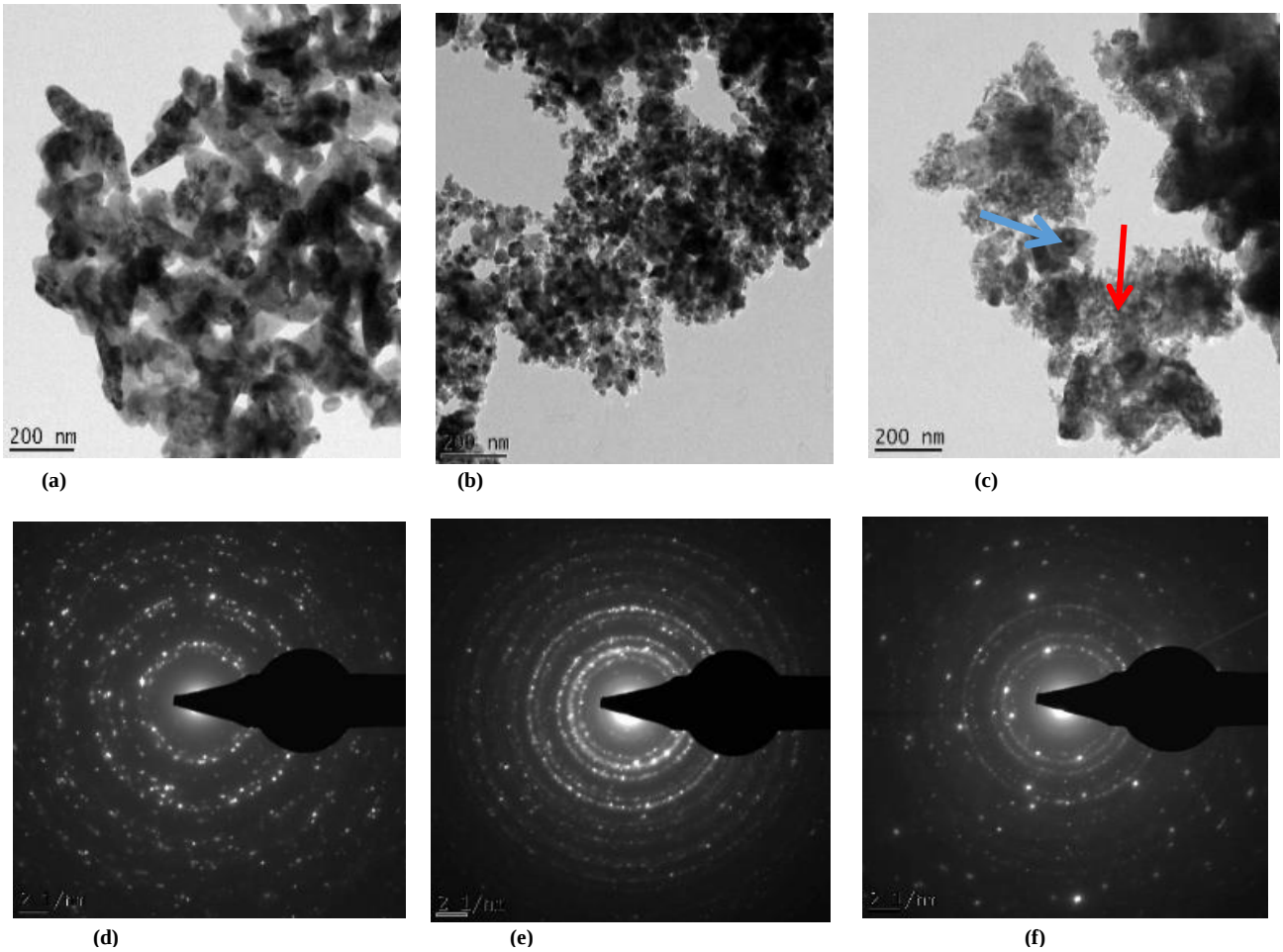

Figure 2: HRTEM images of (a) ZnO (b) $NiFe_2O_4$ (c) 3% $ZnO/NiFe_2O_4$ and SAED patterns of (d) ZnO (e) $NiFe_2O_4$ (f) 3% $ZnO/NiFe_2O_4$

formation of needle-shape $NiFe_2O_4$ with strong degree of agglomeration. The difference in the shape obtained by Zhang et al.,(2009) and Manikandan *et al.* (2018) compared to the hexagonal shape reported in this study may be due difference in synthesis methods. In the case of 3% $ZnO/NiFe_2O_4$, rod-like to spherical nanostructures with little agglomeration were observed with average particle size of 18-24 nm (Figure 2 (f)). The observed trend may be due to the overlap between $NiFe_2O_4$ and ZnO along their direction of growth (Moradmard *et al.*, 2015). The spacing of the lattice fringes was found to be about 0.37 nm for 3%, and thus corresponds to the [311] crystal planes and further confirmed the growing pattern of rods along the direction parallel to the base plane of the ZnO wurtzite structure in a depth of around 28 nm. The SAED pattern also confirmed that the prepared nanocomposites were well crystalline and grown along the [100] and [101] direction. It can be clearly seen (red arrow in Figure 2 (c) that the incorporated $NiFe_2O_4$ coating layer was entrapped on the surface of ZnO for 3% loading. The ferrite core appears with a darker contrast than the ZnO matrix which was entrapped within the core and outer shell of dark core particles. The differences in electron penetration efficiency of bimetallic elements may be responsible for the observed trend. The successful incorporation of Fe and coupling effect of Ni ions onto the lattice layer of ZnO may be responsible for the formation of hetero junctions. Zhu *et al.* (2016) reported the hexagonal morphology of ZnO nanoparticles in the range of 20–350 nm and found that the $NiFe_2O_4$ nanoparticles possess irregular network structures, with an average particle size of approximately 103 nm. In the same study, the authors reported porous brick-like structure of $ZnO/NiFe_2O_4$ composite. Additionally, Moradi *et al.*, (2015) reported the spherical morphology of $ZnO/NiFe_2O_4$ with an average particle size of about 35–45 nm. The difference in the obtained particle size in this study related to previous findings may be attributed to the different synthesis conditions such as calcinations temperature and mixing ratio.

2.) XRD analysis

The phase structures of the three samples were examined using XRD technique and the orientation pattern is shown in Figure 3. Figure 3 (a) show the presence of strong and sharp intense diffraction peaks at 2 theta values of 48.5°, 57.2°, 63.5° and 68.5°. The observed diffraction peaks with corresponding miller indices (100), (002) and (101) matched well with the standard wurtzite phase of ZnO and no other crystalline phase was observed (Zhang *et al.*, 2015). The absence of other phases implies that the ZnO nanoparticles are pure, free of impurities and also crystalline in nature. These crystal planes matched well with hexagonal wurtzite phase of zinc oxide.

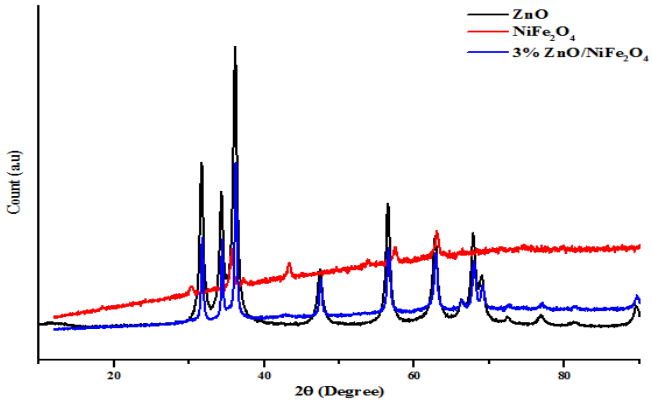

Figure 3: XRD pattern of (a) ZnO (b) $NiFe_2O_4$ (c) 3% ZnO/$NiFe_2O_4$ nanocomposites.

The formation of hexagonal wurtzite structure of ZnO nanoparticles is in accordance with the previously synthesized ZnO nanoparticles using different techniques such as solvo thermal, chemical precipitation, sol-gel among others (Zhu et al. 2016). The mean crystallite size of the nanoparticles (D), were obtained by means of the Debye-Scherrer's equation given as:

$$D = \frac{k\lambda}{\beta cos\theta} \quad (4)$$

where k is a constant (k = 0.94), and λ is the wavelength = 0.1541 nm, θ is the Bragg angle, β is the full width half maximum (FWHW) of the peak at 2θ.

According to the Debye- Scherrer's equation, the crystallite size of ZnO nanoparticles ranges between 13 nm – 28 nm. The XRD pattern of $NiFe_2O_4$ nanoparticles is shown in Figure 3 (b); it revealed the presence of well-defined Bragg's reflections of different intensity at 2θ values of 30.29°, 35.72°, 43.36°, 57.59° and 63.92° with corresponding crystal planes (220), (311), (400), (511) and (440) which depict the formation of high-crystalline $NiFe_2O_4$ nanocrystals. This could be assigned to spinel phase of $NiFe_2O_4$with standard reference number (10-0325) (Manikandan *et al.*, 2018).

The presence of the following crystalline planes (311), (220) and (511) suggest more sensitivity towards the cations on octahedral and tetrahedral structure including the oxygen ion parameters (Zhu *et al.*, 2016). This implies absence of a mixed phase and existence of a cubic structure single-phase of $NiFe_2O_4$ (Alias *et al.*, 2010). Accordingly, the crystallite sizes of the $NiFe_2O_4$ nanoparticles were determined using Scherer's equation (Zhu et al., 2016) and found to range between 25.23 - 30.44 nm. The XRD pattern of 3% ZnO/$NiFe_2O_4$ nanocomposites showed the diffraction peaks at 2θ values of 30.32°, 35.34°, 37.21°, 47.23°, 56.71°, 63.40°, and 67.51° with the following crystal plane (100), (220), (102), (311), (222), (110) and (103) corresponding to hexagonal wurtzite phase of ZnO. This implies successful diffusion of Fe_2O_4 onto the pores of ZnO without distortion or destruction of the phase type of ZnO. The average grain size of the synthesized 3% ZnO/$NiFe_2O_4$ nanocomposites was calculated to be 21.39 nm according to Scherrer's equation.

3.) UV-visible spectroscopic analysis

UV–visible spectroscopic measurements were used to determine the light absorbance behavior of $NiFe_2O_4$, ZnO and 3% ZnO/$NiFe_2O_4$ nanocomposites and evaluate the coupling effect of $NiFe_2O_4$ on ZnO in the wavelength range of 200 – 700 nm.

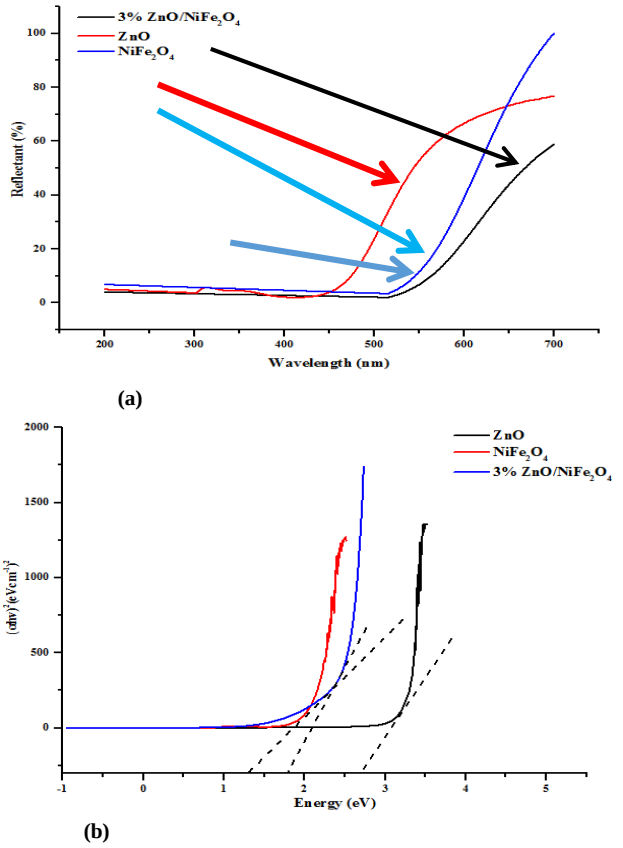

Figure 4: (a) UV-visible spectra and (b) Tauc's Plot of ZnO, $NiFe_2O_4$ and 3% ZnO/$NiFe_2O_4$ nanocomposites.

It was noticed that pure ZnO has an optical-absorption edge at about 455 nm (Fig 4(a)), indicating that the pure ZnO absorb in the visible region. This however contradicts previous reports that established that ZnO nanoparticles absorbed more in the UV region. The differences may be linked to the method of synthesis and the doping effect of carbonaceous species from the plant extract used during the synthesis. $NiFe_2O_4$ nanoparticles absorb at a higher wavelength (505 nm) than ZnO and may be linked to the magnetic properties of nickel and iron respectively. It was also observed that the light absorbance curve of the 3% ZnO/$NiFe_2O_4$ nanocomposites shifted to a longer wavelength compared to ZnO alone. The red shift and broad absorbance in the visible light region for ZnO/$NiFe_2O_4$ nanocomposites, suggested that the coupled

structure may be a highly efficient visible light driven photocatalyst than the individual ZnO and $NiFe_2O_4$ respectively (Zhu *et al.*, 2016).

Figure 4 (b) further revealed a substantial reduction of the photo-electron-hole recombination rate of ZnO by $NiFe_2O_4$. The 3% ZnO/$NiFe_2O_4$ has a smaller band gap of 1.35 eV, which is an evidence of improved catalytic activity compared to pure ZnO and $NiFe_2O_4$ with band gap energies of 2.68 eV and 1.85 eV respectively. The reduction in the band gap energy may be due to the introduction of acceptor energy levels below the conduction level of ZnO. Therefore, 3% ZnO/$NiFe_2O_4$ nanocomposites may have higher solar energy conversion efficiency than that of the pure ZnO and $NiFe_2O_4$, thus leading to enhance photocatalytic activity of the ZnO.

4.) BET analysis

The surface area, pore volume and pore size of the synthesized ZnO, $NiFe_2O_4$ and ZnO/$NiFe_2O_4$ were determined using multiple-plot BET analysis and the result is shown in Table 1 while Figure 5 depicts the N_2 adsorption–desorption curve of various prepared nanomaterials.

Table 1: Surface Area, Pore Volume and Pore Size Distribution of the Synthesized Photocatalyst.

Sample	Surface area (m^2/g)	Pore vol. (cc/g)	Pore diameter (nm)
ZnO	8.988	0.353	13.173
$NiFe_2O_4$	40.387	0.214	10.099
ZnO/$NiFe_2O_4$	44.693	0.190	8.113

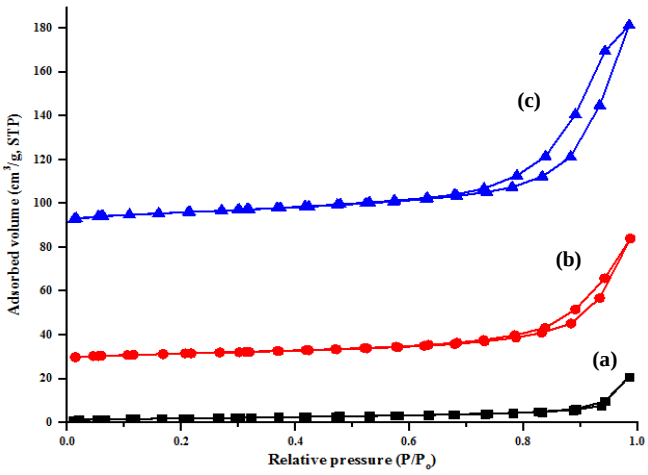

Figure 5: BET N_2 adsorption–desorption isotherms (a) ZnO (b) $NiFe_2O_4$ (c) 3% ZnO/$NiFe_2O_4$ Nanomaterials.

The isotherms of $NiFe_2O_4$ and 3% ZnO/ $NiFe_2O_4$ nanomaterials shown in Figure 5 according to the IUPAC classification belongs to type IV with a narrow hysteresis loops (Xu *et al.*, 2013). This indicates that the $NiFe_2O_4$ and 3% ZnO/$NiFe_2O_4$ nanocomposites were mesoporous in nature (Zhu *et al.*, 2016). While, that of ZnO nanoparticles was assigned as type II isotherm, which is an evidence of the macroporous nature of ZnO as seen in the curve (Zhu *et al.*, 2016). The enhancements in the surface area of ZnO photocatalyst was due to the addition of $NiFe_2O_4$ especially which suggest the existence of synergetic effect between the two materials. The narrow pore size distribution with average pore diameter of 8.11 nm for ZnO/$NiFe_2O_4$ composites compared with ZnO and $NiFe_2O_4$ alone as shown in Table 1 further confirmed enhanced mesoporosity nature of the coupled ZnO/$NiFe_2O_4$. The coupling effects between $NiFe_2O_4$ and ZnO nanoparticles which resulted to formation of hetero-junctions may be responsible for the narrower pore size distribution and smaller pore diameter in ZnO/$NiFe_2O_4$ composites. Again, the mesoporosity nature and higher surface area of ZnO/$NiFe_2O_4$ composites are evidence of more active binding sites and free reactive species in ZnO/$NiFe_2O_4$ than ZnO and $NiFe_2O_4$ alone.

5.) XPS analysis

The surface oxidation state of the elements in ZnO, $NiFe_2O_4$ and ZnO/$NiFe_2O_4$ nanocomposites were examined by XPS and the result of the general survey is shown in Figure 6 (a-f).

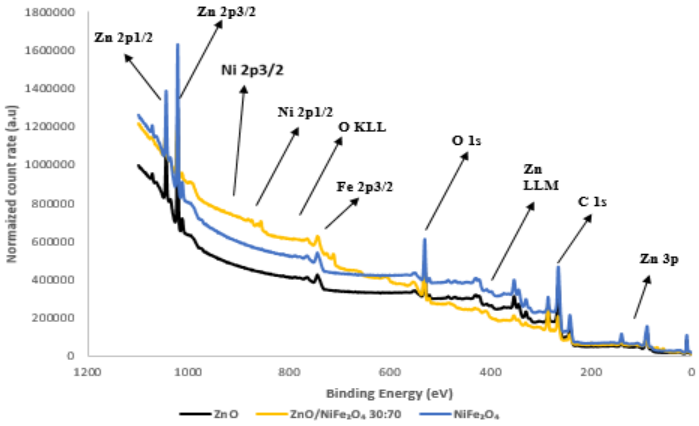

Figure 6(a). XPS general survey of the three prepared nanomaterials.

From Figure 6 (a), it was observed that the major elements in ZnO are Zn and O. In the case of $NiFe_2O_4$ and ZnO/ $NiFe_2O_4$ nanocomposites Ni, Fe, Zn, O and C were detected at different binding energies and their corresponding orbital types were 2p, 2p, 2p, 1s and 1s respectively. The detected carbon originated from plant extract used during the synthesis. The

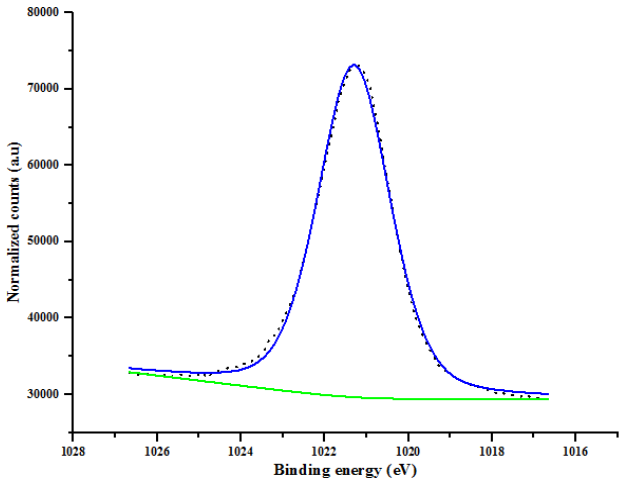

Figure 6(b): High resolution spectrum of Zn $2p_{3/2}$ orbital.

high-resolution spectra of the individual elements are displayed in Figure 6 (b-f).

The (2p core level) of ZnO nanoparticles revealed one sharp and dominant peak located at the binding energy of 1021.3 eV. The peak belongs to the Zn $2p_{3/2}$ orbital and confirmed the existence of Zn in +2 oxidation state (Xu *et al.*, 2013). Figure 6(c) which represents the O 1s orbital in ZnO revealed the presence of O bonded to Zn and C in the binding energy region of 531.5 and 532.7 eV respectively. This suggests the formation of Zn-OH and C=O bond respectively. The energy position of the Zn $2p_{3/2}$ peak (1021.3 eV) as well as the energies and shape of the oxygen peak indicate that the ZnO nanoparticles are rod like in shape (Zhu *et al.*, 2016).

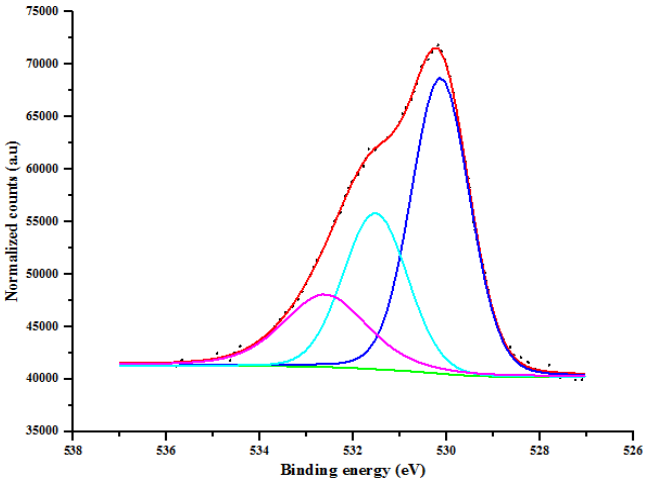

Figure 6(c): Detailed XPS spectrum of the O 1s energy region in ZnO.

As shown in Figure 6 (d), Ni $2p_{3/2}$ and Fe $2p_{3/2}$ envelopes were fitted with empirical fitting parameters considering the unique peak shape of the Ni-ferrite in both the Ni $2p_{3/2}$ and Fe $2p_{3/2}$ regions. The peak with binding energy of 709.0 eV was ascribed to the Fe^{3+} cation located at the octahedral site. While the binding energy of 710.2 eV attributed to Fe^{2+} cations was located at the tetrahedral site in the spinel structure

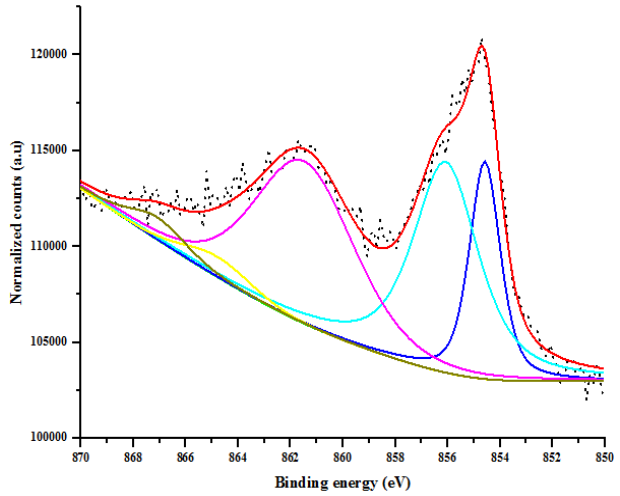

Figure 6(d): Empirical fits for the Ni $2p_{3/2}$ XPS energy envelope in $NiFe_2O_4$.

(Yurddaskal *et al.*, 2017). The binding energy values of Ni $2p_{1/2}$ and Ni $2p_{3/2}$ peaks was found to be 854.1 eV and 867.0 eV respectively and O 1s peak was noticed at binding energy value of 527.4 eV which correspond to O^{2-} ion in the material.

Figure6 (e) shows the empirical fits for the Fe $2p_{3/2}$ envelop in $NiFe_2O_4$. To separate the Fe^{3+} and Fe^{2+} contributions the following assumption were made: The empirical multiplet splits used for fitting the Fe $2p_{3/2}$ peak in Fe_3O_4 are also applicable to $NiFe_2O_4$. The same relative ratios to Ni, peak positions and FWHMs were used. Neither the "surface peak" at 715.9 eV nor the "pre peak" at 707.8 eV was considered in calculating the relative ratios (Yong and Zhong, 2015).

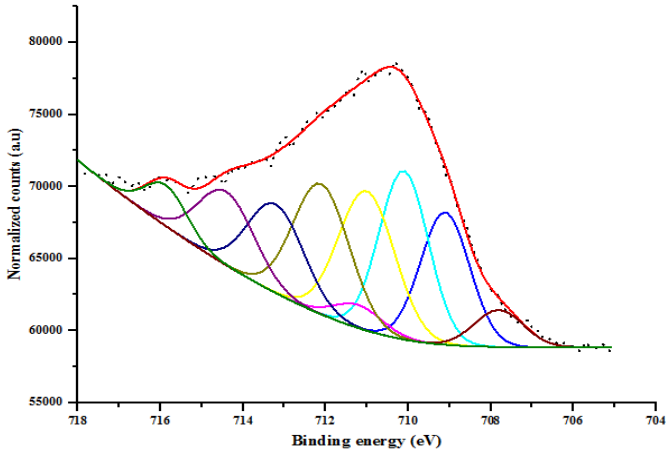

Figure 6(e): Empirical fits for the Fe $2p_{3/2}$ XPS energy envelope in $NiFe_2O_4$.

In Figure 6(f), the Zn $2p_{3/2}$ peaks were fitted with two peaks (FWHM 2.2 eV) and separated by 1.6 eV. The peak at 1021.7 eV is ascribed to the formation of zinc ferrite with zinc atoms occupying tetrahedral sites. The peak at 1023.2 eV is possibly Zn at octahedral sites (Song *et al.*, 2014).

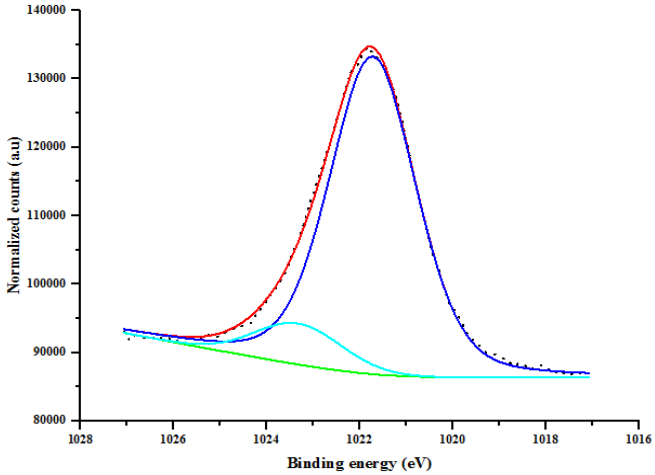

Figure 6(f): Detail XPS spectra and fits for specimens Zn, Ni, Fe, O in 3% ZnO/$NiFe_2O_4$.

B. *Treatment of Tannery Wastewater*

The result of the physico-chemical analysis of selected parameters in the tannery wastewater prior to adsorptive and photocatalytic treatment by the nanocomposite is shown in Table 2.

Table 2: Physiochemical parameters of tannery wastewater before treatment.

Indicator Parameters (mg/L)	Tannery wastewater	Standards	
	Before Treatment	WHO	NIS
BOD	1471.3	30	50
COD	1684.8	250	500
TOC	788.7	5	40
SO_4^{2-}	313.9	100	100
NO_3^-	262.5	40	50
Cl^-	957.1	1000	600

NESREA: National Environmental Standards and Regulations Enforcement Agency (2015); WHO = World Health Organization (2016)

It is obvious from table that the tannery wastewater is highly polluted with organic and inorganic materials due to the high value of the indicator parameters relative to the permissible limits of the two standards used. Thus, the wastewater needs to be treated before discharge into water bodies or environment. The results of the treatment of the tannery wastewater via adsorptive and catalytic method by three materials are shown in Figure 7 (a) – (c).

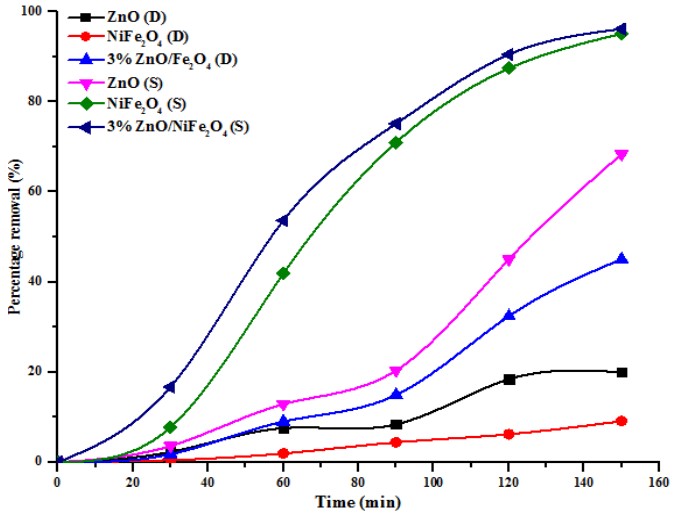

Figure 7(a): Removal and Degradation Efficiency of TOC in tannery wastewater by ZnO, $NiFe_2O_4$ and ZnO/$NiFe_2O_4$ (S = sunlight, D= darkness).

As shown in Fig 7 (a-c), it can be noticed that when the material was used in the presence of natural light from the sun, there was a significant reduction of the indictor parameters

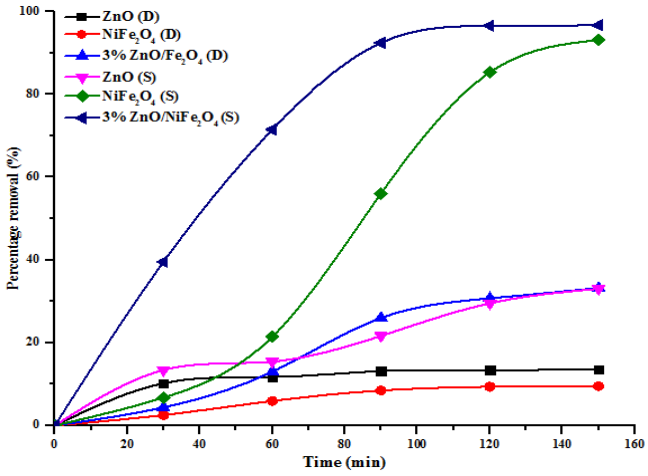

Figure7 (b). Removal and Degradation Efficiency of COD in tannery wastewater by ZnO, $NiFe_2O_4$ and ZnO/$NiFe_2O_4$ (S = sunlight, D = darkness).

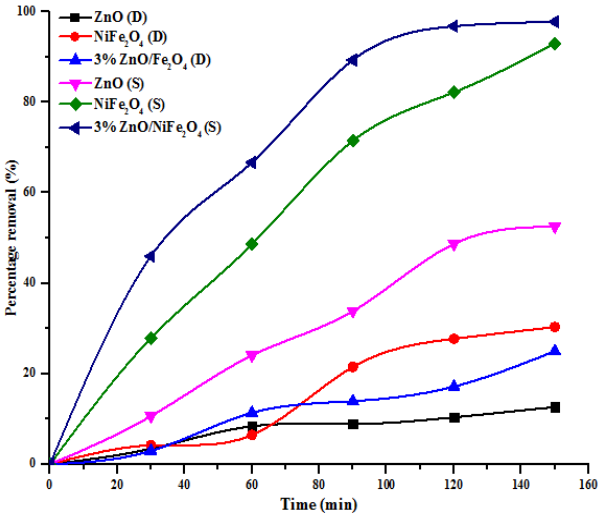

Figure7(c). Removal and Degradation Efficiency of BOD in tannery wastewater by ZnO, $NiFe_2O_4$ and ZnO/$NiFe_2O_4$ (S = sunlight, D = darkness)

compared to the when the material was used in the absence of natural light from the sun. This implies that the prepared nanomaterials behave more as nanocatalyst than as nanoadsorbent. The catalytic results demonstrated that as the irradiation time increases the mineralization rate also increases. It was generally noticed that at every contact time, the mineralization rate of the organic pollutants in the tannery wastewater almost double the removal efficiency by the same nanomaterials. The degradation efficiency of the organic pollutants in the tannery wastewater expressed in term of TOC using 3% ZnO/$NiFe_2O_4$ was 96.15% after 150 min. While that of $NiFe_2O_4$ and ZnO nanoparticles were 85.86% and 68.40% respectively. Similar trend was observed for COD reduction with 95.82%, 85.31%, and 69.35% for 3% ZnO/$NiFe_2O_4$, $NiFe_2O_4$ and ZnO nanoparticles. For BOD reduction, 97.78%,

79.68%, 52.55% mineralization efficiency was noticed for 3% ZnO/NiFe$_2$O, NiFe$_2$O$_4$ and ZnO respectively.

In Figure 7 (a-c) it was noticed that the adsorptive performance of the three materials with respect to the reduction of TOC, COD and BOD level in the tannery wastewater was in the order of 3% ZnO/NiFe$_2$O$_4$ > NiFe$_2$O$_4$ > ZnO. It was also noticed that, increase in the contact time corresponds to an increase in the removal efficiency of the indicator parameters (TOC, COD and BOD by the nanomaterials. Similar trend was observed when Zhu *et al.*, (2016) evaluated the photocatalytic performance of NiFe$_2$O$_4$/ZnO materials through the Congo Red (CR) decolorization under simulated solar light irradiation. The decolorization efficiency (%) of (CR) solution by NiFe$_2$O$_4$/ZnO hybrids, ZnO, m-NiFe$_2$O$_4$/ZnO, and NiFe$_2$O$_4$ under simulated solar light irradiation for 10 min were 94.55%, 64.69%, 29.05% and 7.84%, respectively.

The decolorization of CR solution by the NiFe$_2$O$_4$/ZnO dramatically improved when compared with those of the other materials. The improved photocatalytic performance of the 3% ZnO/NiFe$_2$O$_4$ loading in this work may be due to the improved surface area and band gap energy (Song *et al.*, 2014). It was generally noticed that complete removal/degradation of the indicator parameters by the prepared nanomaterial was not achieved. This may be linked to the presence of radical scavengers such as NO_3-, SO_4^-, and Cl^- which inhibited the performance of the nanocatalyst due to strong competition with the hydroxyl radicals (Udom *et al.*, 2013). The enhanced photocatalytic and adsorptive efficiency of 3% ZnO/NiFe$_2$O$_4$ may be attributed to its low band gap energy (1.35 eV) and higher surface area 44.374 m^2/g. This is however 5 and 1.13 times greater than the surface area of ZnO and NiFe$_2$O$_4$ respectively. The close coupling of ZnO/NiFe$_2$O$_4$ nanocomposites also enhanced the electron transfer rate between interfaces and prevented the recombination of photo-generated electrons and holes

IV. CONCLUSION

In conclusion, the coupling of NiFe$_2$O$_4$ onto the lattice structure of ZnO influenced the band gap energy and surface area which enhanced the suppression of electron-hole recombination rate of ZnO. 3% ZnO/NiFe$_2$O$_4$ exhibited the most improved photodegradation and removal of the organic molecules in tannery wastewater compared to ZnO and NiFe$_2$O$_4$ alone. This study demonstrated that the prepared nanomaterials played a dual role as nanoadsorbent and photocatalyst which can be attributed to the formation of ZnNiFeO$_4$. The future work will focus on the proper optimization of photocatalytic degradation and adsorption parameters such as variation of catalyst dosage, volume of the wastewater, stirring speed, stirring time, and temperature

ACKNOWLEDGEMENTS

The authors wish to acknowledge the following collaborators for their assistance in the analysis of the prepared nanomaterials: Dr. Franscious Cummings of Electron Microscope Unit, Department of Physics, University of the Western Cape, South Africa for the HRSEM and HRTEM analysis; Prof. W.D. Roos, Department of Physics, University of the Free State, South Africa.

REFERENCES

Abdel, E.A.; F.E. Farghaly; R.T. AbdelWahed and M.F. El-Shahat. (2015). Treatment of Industrial Wastewater Using Advanced Oxidation Processes. International Journal of Scientific in Agricultural Sciences, 2(1): 68–78.

Alias, S.S.; A. B. Ismail and A.A. Mohamad (2010). Effect of pH on ZnO nanoparticle properties synthesized by sol–gel centrifugation. Journal of Alloys and Compounds, 499: 231–237.

Angadi, V.J.; B. Rudraswamy; K. Sadhana; S. Ramana; S. Murthy and K. Praveena. (2016). Effect of Sm^{3+}-Gd^{3+} on structural, electrical and magnetic properties of Mn-Zn ferrites synthesized via combustion route. Journal of Alloys and Compounds, 656: 5-12.

Asim, N.; M. Badeiei; K.B. Ghoreishi; A. Ludin; M.R.F. Zonooz and K. Sopian. (2013). New developments in photocatalysts modification: case study of WO_3. Advances in Fluid Mechanics and Heat & Mass Transfer, 1109-116.

Brintha, S.R. and Ajitha, M. (2015). Synthesis and characterization of ZnO nanoparticles via aqueous solution, sol-gel and hydrothermal methods. Journal of Applied Chemistry, 8(11): 66-72.

Chen, D.; F. Fan-Zhang; Q. Li; W. Wang; G. Qian; Y. Jin and Z. Xu. (2016). A promising synergistic effect of nickel ferrite loaded on the layered double hydroxide-derived carrier for enhanced photocatalytic hydrogen evolution. International Journal of Hydrogen Energy, 1-9.

Hassan, S.S. (2015). A Review on Nanoparticles: Their Synthesis and Types. Research Journal of Recent Science, 4(2): 9-11.

Hayelom, D. and Adhena, A. (2014). Tannery Waste Water Treatment: A Review. International Journal of Emerging Trends in Science and Technology, 1(9): 1488-1494.

Hazra, S. and Ghosh, N.N. (2014). Preparation of nanoferrites and their applications. Journal of Nanosciene and Nanotechnology, 14: 1983-2000.

Hushim, M.; S.E. Alimuddin; S. Shirsath; R. Kumar; A.S. Kumar; J. Roy; R.K. Shah and K. Kotnala. (2013). Preparation and characterization chemistry of nanocrystalline Ni-Cu-Zn ferrite. Journal of Alloys Compounds, 549: 348-357.

Islam, B.I.; A.E. Musa; E.H. Ibrahim; A.A. Salma; B.C. Sharafa and M.E. Babiker. (2014). Evaluation and Characterization of Tannery Wastewater. Journal of Forest Products & Industries, 3(3): 141-150.

Kumaran, N.N. and Muraleedharan, A. (2017). Photocatalytic activity of ZnO and Sr^{2+} doped ZnO nanoparticles. Journal of Water Process Engineering, 17: 264-270.

Manikandan, V.; J.C. Denardin; S. Vigniselvan and R.S. Mane. (2018). Structural, dielectric and enhanced soft magnetic properties of lithium (Li) substituted nickel ferrite ($NiFe_2O_4$) nanoparticles. Journal of Magnetism and Magnetic Materials, 2(1): 34-42.

Manokari, M.; C.P. Ravindran and M.S. Shekhawat. (2016). Production of Zinc Oxide Nanoparticles using aqueous extracts of a medicinal plant *Micro coccamercurialis* (L.) Benth. World Scientific News, 30: 117-128.

Matinise, N.; X.G. Fuku; K. Kaviyarasu; N. Mayedwa and M. Maaza. (2017). ZnO nanoparticles via Moringa oleifera green synthesis: Physical properties & mechanism of formation. Applied Surface Science, 406: 339–347.

Moradmard, H. and Farjami, S.S. (2015). The Variation of Magnetic Properties of Nickel Ferrite by Annealing Manufacturing Science and Technology, 3(4): 141-145.

Nigerian Industrial Standard (NIS). (2015). Nigerian Standard for Drinking Water Quality, 16- 17.

Pawar R.C., Kim, H., and Lee, C.S. (2014). Defect-controlled Growth of ZnO Nanostructures Using its Different Zinc Precursors and Their Application for Effective Photodegradation," Current Applied Physics, 14(4): 621-629.

Peruma, S.; C.G. Sambandam; K.M. Prabu and S. Ananhakumar. (2014). Synthesis and Characterization studies of Nano TiO_2 prepared via Sol-Gel Method. Journal of Ovonic Research, 5(1): 34-94.

Ramachandra, R.A.; A.N. Mallika; B.K. Sowri and R.K. Venugopa. (2015). Hydrothermal Synthesis and characterization of ZnO Nano Crystals. International Journal of Mining, Metallurgy and Mechanical Engineering, 3(2): 2320-4060.

Sena, R. and Jainb, P. (2015). Synthesis and Characterization of nickel ferrite ($NiFe_2O_4$) nanoparticles prepared by sol- gel method," Materials Today: Proceedings, 2: 3750 -3757.

Snehal, Y.; M. Chandra and M. Prakash. (2016). Biosynthesis of Zinc Oxide Nanoparticles Using *Ixora Coccinea* Leaf Extract—A Green Approach. Open Journal of Synthesis Theory and Applications, 5: 1-14.

Song, S.; Q. Song; J. Li; V. Raman and Z.M. Zhongyi. (2016). Characterization of submicrometer-sized NiZn ferrite prepared by spark plasma sintering. Ceramics International, 40: 6473-6479.

Suresh, B.K. and Narayanan, V. (2013). Hydrothermal Synthesis of Hydrated Zinc Oxide Nanoparticles and its Characterization. Chemical Science Transactions, 2(1): 33-36.

Swaroop, K. and Somashekarappa, H.M. (2015). Effect of pH values on surface Morphology and Particle size variation in ZnO Nanoparticles Synthesised by co-precipitation Method. Research Journal of Recent Sciences, 4: 197-201.

U.S. Environmental Protection Agency (EPA). Cincinnati, OH (2009). Method 415.3: Determination of Total Organic Carbon and Specific UV Absorbance at 254 nm in Source Water and Drinking Water. Revision 1.2. Document no. EPA/600/R-09/122

Udom, I.; M.K. Ram; E.K. Stefanakos; A.F. Hepp and D.Y. Goswami. (2013). One dimensional ZnO nanostructures: Synthesis, properties and environmental applications. Material Science Semiconductor Process, 16: 2070-2083.

Wang, H.; B. Seonghoon; L. Jonghyuck and L. Sangwoo. (2009). High photocatalytic activity of silver-loaded ZnO-SnO_2 coupled catalysts. Chemical Engineering Journal, 146(9): 355-361.

WHO World Health Organization (2016). Geneva Switzerland. Guidelines for Drinking Water Quality, 4th edition. 2016

Wosnie, A.; A. Wondie and B. Dar. (2014). Tannery Effluent Characterization and its Impact on the Head of Blue Nile River. African Journal of Environmental Science and Technology, 8(6):.312-318.

Xu, S.; D. Tan; D. Bi; H.P. Shi; W.S. Lu and F. Wen. (2013). Effect of Magnetic Carrier $NiFe_2O_4$ Nanoparticles on Physicochemical and Catalytic Properties of Magnetically Separable Photocatalyst $TiO_2/NiFe_2O_4$. Chemical Research in Chinese Universities, 29(1): 121-125.

Yong, D. and Zhong, L.W. (2015). Electron energy-loss spectroscopy study of ZnO nanobelts. Journal of Electron Microscopy, 54(3): 287-291.

Yurddaskal, M.; Y. Serdar; D. Tuncay; M. Yurddaskal; E. Mustafa; A. Idil and C. Erdal. (2017). Enhanced photocatalytic properties of Sn-doped ZnO nanoparticles by flame spray pyrolysis under UV light irradiation. Journal of Turkish Chemical Society, 5(1): 15-22.

Zhang, G.; X. Wanbang; L. Zheng; H. Weiqing and W. Yongxian. (2009). Preparation and characterization of multi-functional $CoFe_2O_4$–ZnO nanocomposites. Journal of Magnetism and Magnetic Materials, 321: 1424-1427.

Zhang, J.; T. Liu; Y. Zhang; W. Zeng; F. Pan and X. Peng. (2015). Hydrothermal Synthesis and Growth Mechanisms of Different ZnO Nanostructures and their Gas-sensing Properties. Journal of Material Science: Mater Electron, 26: 1347–1353.

Zhu, Y. H.; J. Ru; F. Yong-Qian; L. Rong; Y. Jun and J. Sheng-Tao. (2016). Novel multifunctional $NiFe_2O_4$/ZnO hybrids for dye removal by adsorption, photocatalysis and magnetic separation. Applied Surface Science, 369: 110.

Zulfiqar, A.M.N.; K.B. Chandrasekhar; A. A. Jahagirda; H. Nagabhushana and B.M. Nagabhushan. (2015). Photocatalytic activity of nanocrystalline ZnO, α-Fe_2O_3 and $ZnFe_2O_4$/ZnO. Applied Nanoscience, 5: 961–968.